J Mater Sci (2012) 47:1119–1126
DOI 10.1007/s10853-011-5883-z

MATERIALS IN NEW ZEALAND

Effect of annealing on the structural, electrical and magnetic properties of Gd-implanted ZnO thin films

P. P. Murmu · J. Kennedy · B. J. Ruck · G. V. M. Williams · A. Markwitz · S. Rubanov · A. A. Suvorova

Received: 21 February 2011 / Accepted: 17 August 2011 / Published online: 31 August 2011

Abstract We report the results from structural, electrical and magnetic measurements on Gd-implanted ion beam deposited zinc oxide (ZnO) films. 40 keV Gd ions were implanted into 150 nm thick ZnO films with fluence 2.8×10^{15} cm^{-2}. RBS spectra reveal the implanted atoms are located in the near-surface region in as-implanted and up to 923 K annealed films, diffusing deeper into the films after 1073 K annealing. SEM images show that the average grain size increases from 10 to 30 nm upon annealing. High-resolution and energy-filtered transmission electron microscopy of a ZnO:Gd sample annealed at 923 K reveal the presence of Gd-rich regions in the film, but no evidence of pure Gd precipitates. Annealing increases the resistivity, and the carrier concentration decreases by as much as six orders of magnitude after annealing at up to 1073 K. All annealed films display a mix of paramagnetic, superparamagnetic and ferromagnetic behaviour extending to temperatures above 300 K that we attribute to the spatially inhomogeneous Gd distribution. The paramagnetic behaviour can be attributed to isolated Gd moments, while the ordered magnetic phases appear to arise from Gd-rich regions within the ZnO. X-ray absorption near edge spectroscopy provides evidence that there exist oxygen vacancies.

P. P. Murmu · J. Kennedy (✉) · A. Markwitz
National Isotope Centre, GNS Science, P.O. Box 31312, Lower Hutt, New Zealand
e-mail: j.kennedy@gns.cri.nz

P. P. Murmu · B. J. Ruck
School of Chemical and Physical Sciences, Victoria University of Wellington, P.O. Box 600, Wellington, New Zealand

P. P. Murmu · J. Kennedy · B. J. Ruck · G. V. M. Williams · A. Markwitz
The MacDiarmid Institute for Advanced Materials and Nanotechnology, Wellington, New Zealand

G. V. M. Williams
Industrial Research Limited, P.O. Box 31310, Lower Hutt, New Zealand

S. Rubanov
Inst Bio21, University of Melbourne, Melbourne, VIC 3010, Australia

A. A. Suvorova
Centre for Microscopy, Characterization and Analysis, The University of Western Australia, Crawley, WA 6009, Australia

Introduction

Dilute magnetic semiconductors (DMSs) aim to control the charge and spin degrees of freedom in the same material, with potential applications in the field of "Spintronics" [1]. This can be realized by doping impurity magnetic atoms (transition metal or rare earth (RE) elements) which display ferromagnetic coupling, while still maintaining the conventional semiconducting characteristics. Several mechanisms have been proposed for long range indirect ferromagnetic interactions among doped magnetic impurity atoms (e.g. Zener [2], Anderson [3], Ruderman–Kittel–Kasuya–Yosida (RKKY) [4] or F-centre exchange [5] models). Initially, III–V materials were investigated due to the already established electronic applications [6]. However, low ferromagnetic transition temperatures (T_C) (e.g. $\sim$170 K for GaAs:Mn) motivated researchers to seek alternate DMS systems which exhibit ferromagnetism above room temperature. Dietl et al. [2] predicted that T_C could be greater than room temperature in p-type ZnO doped with Mn. This is particularly interesting because

ZnO has the advantage that it is a direct band gap semiconductor, and it may be easier to integrate the magnetic and optoelectronic properties to create new devices [7]. Further reports of high T_C values in transition metal (V, Cr, Mn, Fe, Co and Ni) doped ZnO [8] triggered several experimental studies, with ferromagnetic transition temperatures as high as ~790 K being reported [9]. However, there remains dispute over the origin of the room temperature ferromagnetic ordering. In some cases it may be due to secondary phases and/or metallic clusters [10]. Furthermore, there are contradicting reports of the magnetic properties in similar systems. For example ZnO:Co systems are reported to exhibit ferromagnetism [11], antiferromagnetism [12], paramagnetism [13], and even the absence of any magnetic moment [14]. Considerable variations in the reported results reflect the sensitivity of the magnetic properties to the sample fabrication techniques and post-growth treatments. The report of ferromagnetic exchange even in un-doped ZnO suggests that the intrinsic defects can significantly contribute towards the ferromagnetic properties [15].

Rare earth elements are interesting dopants in ZnO that are alternatives to transition metal dopants. In RE elements, the 4*f* electrons are strongly localised, so any exchange interactions must be indirect. RE elements (e.g. Gd, Er) are reported to induce ferromagnetic order in ZnO [16–20]. Gd doped into ZnO single crystals and thin films is reported to display ferromagnetic order [17–19]. Ungureanu et al. [18] noticed that electron doping enhances the coupling, a result supported by recent theoretical studies [20]. Potzger et al. [17] reported that a sufficient Gd concentration and activation of charge carriers are required to induce ferromagnetic order in ZnO:Gd. However, annealing can lead to segregation of metallic clusters and/or secondary phases. Thus, it is of particular interest to investigate the effect of annealing temperature on the microstructural, electrical and magnetic properties of ZnO:Gd films. Ion implantation is an established mature technique which has been used to dope RE and other elements into ZnO materials [17, 21, 22]. The ions can be doped to a precise depth and concentration. We have previously described the structural and compositional properties of RE elements implanted into ZnO for potential spintronic applications [23]. This article reports the results from Gd implantation into ZnO films and the effect of annealing at different temperatures on the structural, electrical and magnetic properties.

Experimental procedure

Polycrystalline *c*-axis oriented ZnO thin films of thickness 150 ± 10 nm were deposited onto silicon (100) and thermally oxidised silicon dioxide (SiO_2/Si) substrates using ion beam sputtering [24]. The films were subsequently implanted at room temperature with 2.8×10^{15} Gd cm^{-2} at the dual ion implantation facility at GNS Science, Lower Hutt, New Zealand [25]. The ion energy was 40 keV, and the implantation occurred at normal incidence. Dynamic-Trim [26] calculations predicted that the Gd atoms are located at an average depth of 13 nm below the surface (see Fig. 1a), corresponding to an atomic concentration of ~2.5 at.% with a longitudinal straggling of 6 nm. The implanted films were subsequently annealed at various temperatures for 30 min in vacuum (base pressure ~ 1×10^{-7} mbar). Rutherford backscattering spectrometry (RBS) measurements were performed, using a collimated 2 MeV He^+ beam, for compositional and depth profiling analysis of the implanted layer. Backscattered particles were collected using a surface barrier detector placed at 165° with a target current ~15 nA. Surface morphologies were examined by a JEOL 6500F field emission scanning electron microscopy (SEM). The structural properties were investigated using an FEI TECNAI TF20 field emission gun transmission electron microscope

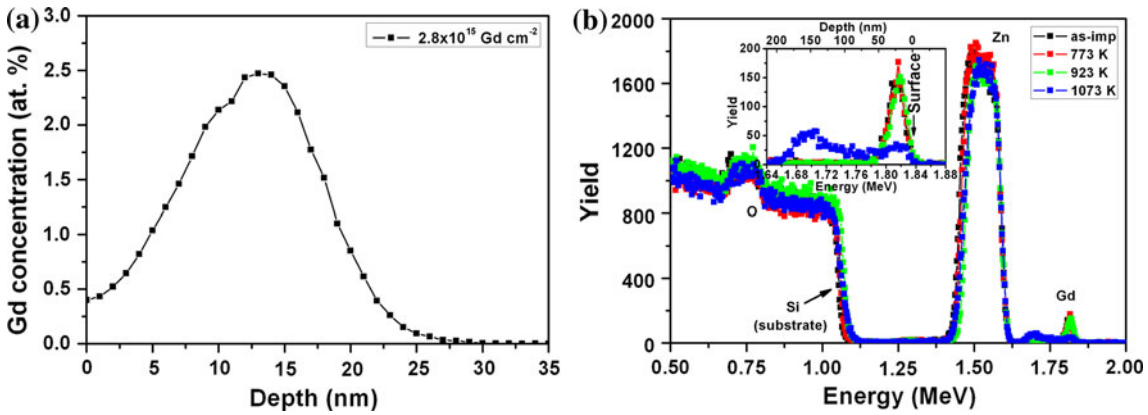

Fig. 1 (Colour online) **a** Gd depth profile calculated with Dynamic-Trim for 40 keV ion energy and 2.8×10^{15} ions cm^{-2}. **b** RBS spectra of 2.8×10^{15} Gd cm^{-2} implanted and annealed ZnO films. The magnified Gd peaks are shown in the *inset*

(TEM) operating at 200 kV. Energy-filtered TEM (EFTEM) imaging was conducted at 200 kV (JEOL, JEM-2100) using an 11Mpix CCD camera (Gatan, Orius1000). Hall-effect and resistivity measurements were carried out at room temperature employing the van der Pauw geometry. Magnetic properties were investigated with a magnetic property measurement system (MPMS) from Quantum Design in the temperature range of 5 to 360 K. Element specific X-ray absorption near edge spectra (XANES) experiments were carried out at the O K-edge and Gd $M_{4,5}$ edges. The spectra were collected in total electron yield (TEY) mode at the Australian synchrotron soft X-ray beam-line.

Results and discussion

Film thickness in number of atoms per unit area and composition were measured with RBS, as shown in Fig. 1b. The energy loss of the ions in the material results in depth profiles of the elements present in the sample, whereas the cross-section (yield of backscattered particles) gives rise to the elemental concentration, and is proportional to the elemental composition [27]. Film thickness and composition were extracted from spectra using the data deconvolution software Rutherford universal manipulation program [28]. The number of Gd atoms in the implanted region (2.71×10^{15} Gd cm^{-2}) was similar to the implanted fluence, which indicates the absence of sputtering during the implantation process. Annealing has significant effects on the re-arrangement of Gd atoms in the implanted layer. At annealing temperatures of up to 923 K the Gd atoms diffuse slightly towards the surface, as shown in the inset to Fig. 1b. However, an opposite trend is observed upon annealing the sample at temperatures greater than 923 K. Here Gd atoms diffuse deeper into the material. Recently, Koskelo et al. [29] reported Co diffusion into ZnO single crystals, and proposed that Co incorporates substitutionally for Zn. Such diffusion appears to apply also to Gd, although the Gd is not necessarily substitutional.

The surface morphology of the Gd implanted and annealed ZnO films was obtained from scanning electron microscopy, as depicted in Fig. 2. It can be seen that the film morphology is homogenous. The average grain sizes for as-implanted and low temperature annealed films are 10 ± 2 and 15 ± 2 nm, respectively. Higher temperature annealing enhances the coalescence of grains, and the average grain size increases up to 30 ± 2 nm at 1073 K.

Cross-sectional TEM (X-TEM) measurements were carried out on un-implanted and Gd-implanted ZnO films. The X-TEM micrograph of the as-deposited film reveals columnar growth. Annealing of the film further enhances the columnar structure, as seen in Fig. 3a for a 2.8×10^{15} Gd cm^{-2} implanted and 923 K annealed ZnO

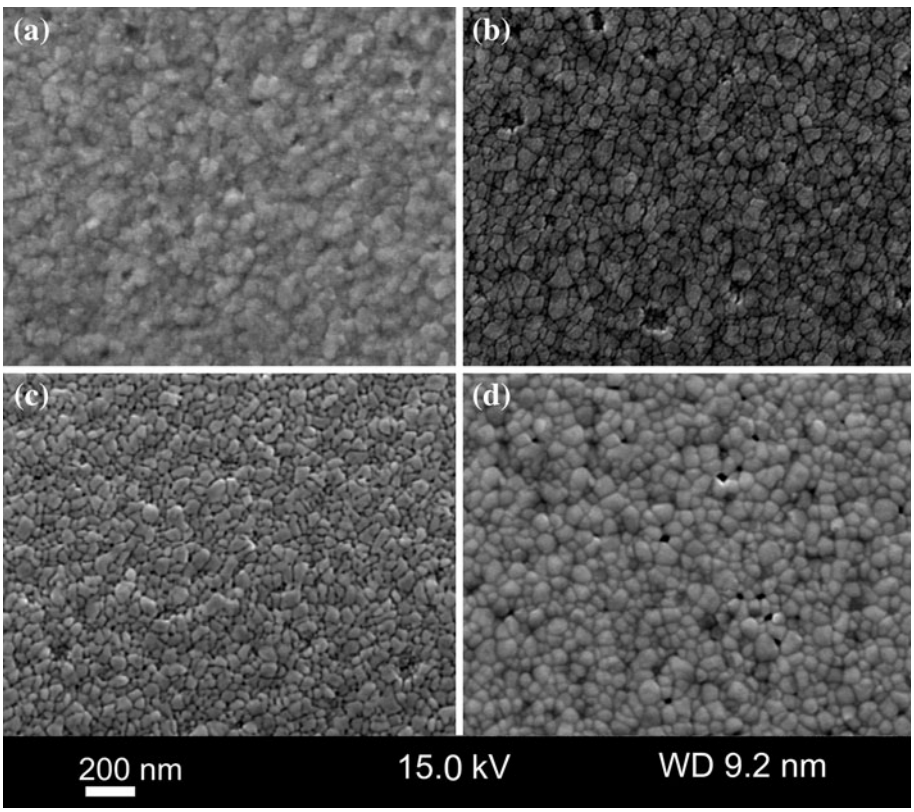

Fig. 2 SEM images of **a** as-implanted, **b** 773 K, **c** 923 K, and **d** 1073 K annealed ZnO:Gd films. The Gd implantation fluence was 2.8×10^{15} Gd cm^{-2}

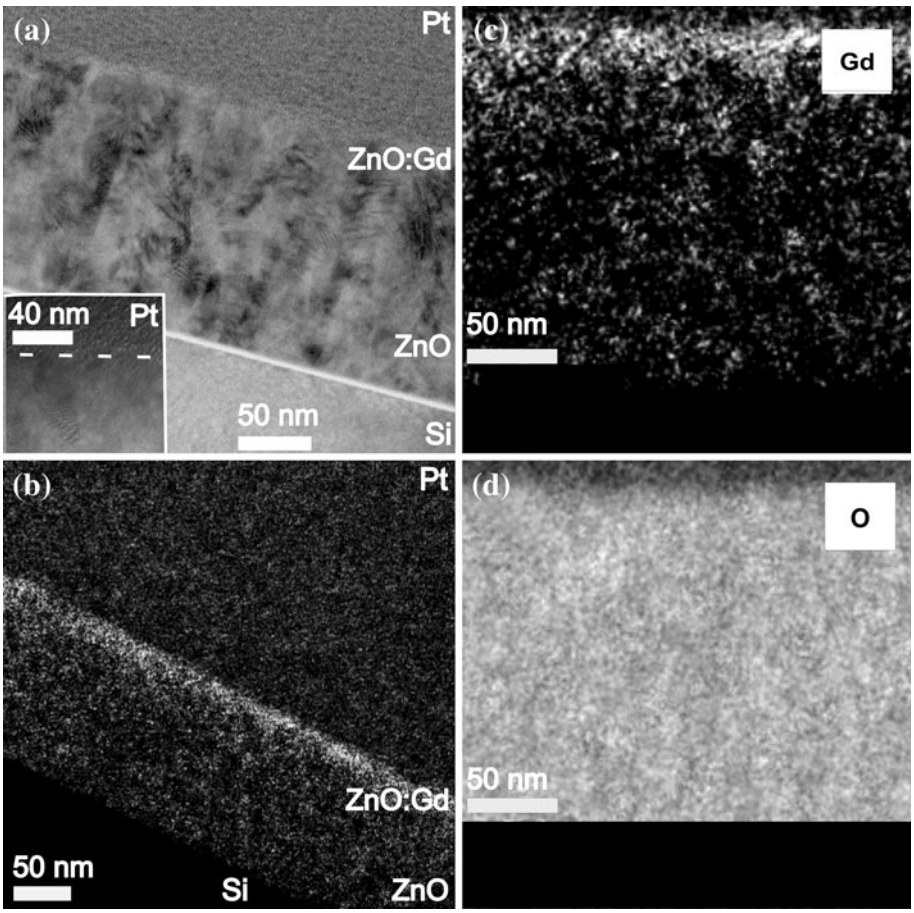

Fig. 3 **a** X-TEM, **b**, **c** EFTEM map of elemental Gd, and **d** EFTEM map of elemental O for a 2.8×10^{15} Gd cm^{-2} implanted and 923 K annealed ZnO film

film. Selected area electron diffraction patterns show that all of the films are polycrystalline. Moire fringes are evident in high-resolution images (Fig. 3a inset), originating due to superposition of ZnO planes in overlapping nanocrystallites. The low resolution image shows evidence of strain within the crystallites, but there is no significant evidence found for the existence of metallic Gd precipitates in either image.

To observe the elemental distribution within the ZnO:Gd film, EFTEM images were acquired for gadolinium, zinc, oxygen and silicon using the standard three window method and the optimum elemental mapping parameters, calculated by use of a reference spectrum. Shown in Fig. 3b is the elemental map for Gd, where it can be observed that most of the Gd atoms are located within about 25 nm of the surface. The high-resolution Gd map shown in Fig. 3c reveals a non-uniform distribution, with nano-sized regions showing enhanced Gd concentration relative to the rest of the surface layer. Element maps for Zn and O (Fig. 3d) do not reveal any significant depleted regions, as might be expected if the Gd were forming metallic clusters. Rather, it appears that the regions of high Gd concentration form within the ZnO lattice without changing the underlying lattice structure. A similar interpretation of the distribution of Co atoms within ZnO:Co has recently been proposed, and used to explain magnetisation and transport properties in that material [30].

The room temperature electrical properties were investigated by Hall-effect measurements using the van der Pauw geometry with an applied magnetic field of 5.5 kOe. Ohmic Au-contacts (thickness $\sim$ 50 nm) were deposited prior to the measurements in an SEM sputter coater system. Figure 4 summarizes the resistivity and carrier concentrations deduced from resistance and Hall-effect measurements in as-deposited and 2.8×10^{15} Gd cm^{-2} implanted and annealed ZnO films. All samples show *n*-type conductivity which is usually attributed to doping by intrinsic defects such as oxygen vacancies or zinc interstitials [31, 32]. The resistivity for the as-deposited film is $\sim 10^{-2}$ Ω cm. After implantation the resistance drops sharply, and applying a two-layer model consisting of the top $\sim$25 nm implanted region and the remaining un-implanted region of the film, we obtain a resistivity for the Gd-implanted layer of about 3×10^{-3} Ω cm.

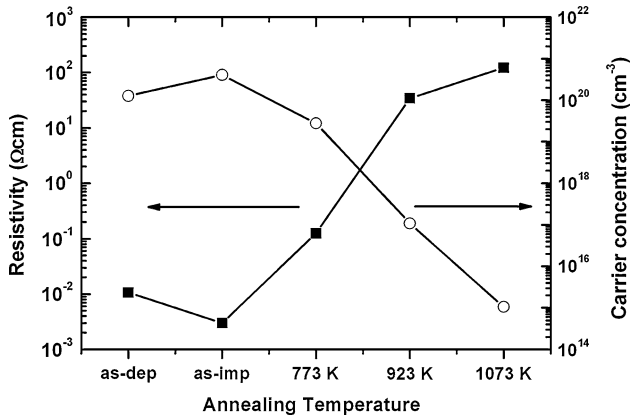

Fig. 4 Resistivity and carrier concentration in as-deposited, 2.8×10^{15} Gd cm^{-2} implanted, and annealed ZnO films

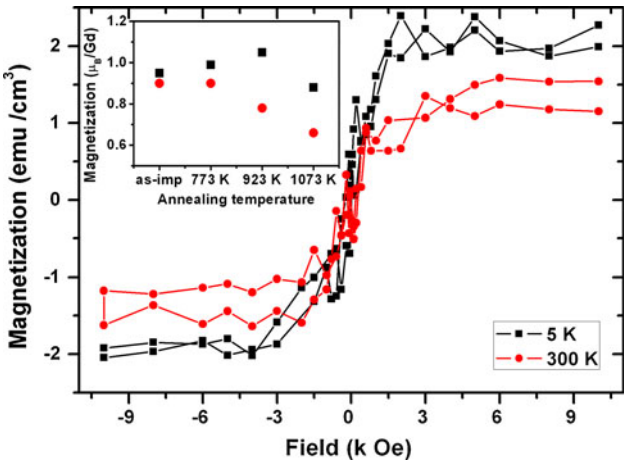

Fig. 5 (Colour online) M(H) curves for a 2.8×10^{15} Gd cm^{-2} implanted and 923 K annealed ZnO film. The *inset* shows the saturation magnetic moment (M_S) for 2.8×10^{15} Gd cm^{-2} implanted films after annealing at different temperatures

This decrease could be due either to conduction via states introduced by the implanted Gd ions themselves, or simply due to an increased carrier concentration associated with implantation-induced defects in the ZnO matrix. Vacuum annealing increases the resistance of the implanted films by up to three orders of magnitude. This is caused by a reduction in carrier concentration which clearly occurs in both the implanted surface region and un-implanted bulk of the film, and indeed a similar increase in resistivity was observed after annealing of un-implanted films. Because both parts of the film undergo significant conductivity changes, the resistivity of the implanted layer was obtained by applying a two-layer model in which the resistivity of the portion of the film below the implantation depth was obtained from measurements on annealed un-implanted films.

Annealing under vacuum or in an oxygen deficient atmosphere is usually expected to increase the concentration of oxygen vacancies, resulting in less resistive films at higher annealing temperatures [18], in contrast to our findings. However, Kim et al. [33] have reported an enhanced resistivity after annealing polycrystalline ZnO films prepared by plasma-enhanced chemical vapour deposition. They suggested that oxygen trapped in grain boundaries can be set free upon thermal annealing. The de-trapped oxygen atoms can compensate the oxygen vacancies present in the films leading to reduced carrier concentration. We believe a similar process is taking place in our un-implanted, Gd implanted and annealed films. The X-ray diffraction spectra (not shown) indeed show better crystalline quality and bigger grain sizes for films after annealing.

Magnetization data are plotted in Fig. 5 for a ZnO film after ion implantation with 2.8×10^{15} Gd cm^{-2} and annealing at 923 K, where the magnetic field was applied parallel to the film surface. Note that the diamagnetic background from the Si substrate was subtracted from the raw data to obtain Fig. 5. The magnetization at 5 and 300 K increases and then saturates above $\sim$2 kOe, which is consistent with the occurrence of ferromagnetic order where the Curie temperature is above 300 K. The resultant saturation magnetic moments, M_S, at 5 and 300 K are 1.05 and 0.75 μ_B/Gd, respectively, where μ_B is the Bohr magneton. Similar measurements were made for different annealing conditions, and the 5 and 300 K saturation moments are plotted in the inset to Fig. 5 as a function of increasing annealing temperature. All of the low temperature saturation moments are considerably less than those found in free Gd^{3+} (7 μ_B/Gd) or Gd metal (7.63 μ_B/Gd) [34]. There is also a small increase in saturation moment per Gd at 5 K with increasing annealing temperature where it is a maximum after the 923 K annealing (1.05 μ_B/Gd) and then it decreases after annealing at higher temperatures. The saturation moments per Gd at 300 K are still a reasonable fraction of the values at 5 K for all annealing temperatures. It is unlikely that the ferromagnetic behaviour up to 300 K can be explained by ZnGd or Gd nanoparticles in the ZnO film. This is because the Curie temperature for ZnGd and Gd metal are 268 [35] and 293 K [36], respectively, while the data in Fig. 5 shows that the Curie temperature in ZnO:Gd is above 300 K. It is possible that there are Gd_2O_3 nanoparticles, but Gd_2O_3 is paramagnetic at room temperature [37].

While the Curie temperature is too high to be explained by ZnGd or Gd nanoparticles, it is apparent from Fig. 6 that a nanostructured magnetic phase exists. Here we plot the zero-field cooled (ZFC) and field cooled (FC) magnetization data at an applied magnetic field of 100 Oe for a film annealed at 923 K. The ZFC data increases until

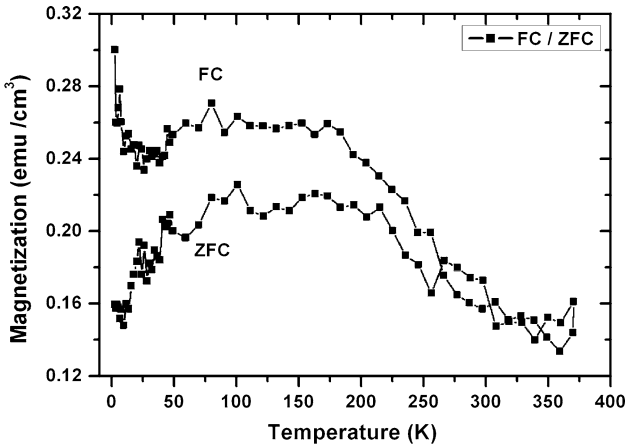

Fig. 6 M(T) curves for a 2.8 × 10^{15} Gd cm^{-2} implanted and 923 K annealed ZnO film. The applied field was 100 Oe

~50 K, is approximately constant until ~200 K, and then it decreases with increasing temperature. The FC data shows a rapid increase with decreasing temperature until ~175 K, followed by a relatively flat magnetization until ~50 K. Below ~25 K, there is a rapid increase in the magnetization. There is also magnetic hysteresis for all temperatures below 300 K. The appearance of magnetic hysteresis and the rapid decrease in the magnetization above ~200 K suggests that there are ferromagnetic nanoparticles where the blocking temperature is ~200 K. The absence of a well-defined peak in the ZFC data indicates that there is a broad distribution in nanoparticle sizes. A significantly smaller magnetic hysteresis is observed from ~200 to 300 K, which could arise from ferromagnetic nanoparticles with sizes large enough that the blocking temperature is above 300 K. The large increase in the FC magnetization below ~25 K likely arises from regions where the Gd moments do not experience long range magnetic ordering, and the resultant magnetic behaviour is paramagnetic down to 5 K. Thus, the analysis of the magnetization shows that there is a non-uniform Gd concentration in the ZnO film, which results in a combination of paramagnetic, superparamagnetic and ferromagnetic behaviour from different regions in the film. Similar spatially inhomogeneous behaviour was also reported in one study of Co in ZnO [38].

The origin of the magnetically ordered phase in ZnO:Gd is not clear. It may be that the RRKY mechanism proposed by Dietl et al. [2] for GaAs:Mn and some other dilute ferromagnetic semiconductors is not appropriate for ZnO:Gd. In this model, the Curie temperature is related to the carrier concentration. However, ZnO:Gd films show a reduction in the carrier concentration by approximately six orders of magnitude while there is no indication that there are significant changes in the Currie temperature. Other explanations include the bound magnetic polarons model [5] where ferromagnetic coupling is mediated by shallow donor electrons. The observed ferromagnetism in ZnO:Co films has been attributed to the existence of Co-rich regions within the ZnO lattice, where the lattice retains its wurtzite structure [30]. Similar behaviour may occur here, and indeed such behaviour is consistent with our TEM results.

The electronic structure of un-implanted and Gd implanted and annealed films was investigated with X-ray absorption near edge spectroscopy. This technique probes un-occupied electronic states in the conduction band and provides element specific information about valence state, site occupancy, and the neighbouring environment. The XANES spectra at the O K-edge are shown in Fig. 7a. The O K-edge involves the transition from O 1s to un-occupied O p-like states, and probes hybridization of oxygen with dispersive Zn and Gd orbitals in the conduction band. The spectra for all samples are similar, and resemble a slightly broadened version of the spectrum expected of single crystal ZnO, where the various features are well reproduced by the oxygen p-projected density of unfilled states obtained from electronic band structure calculations [39].

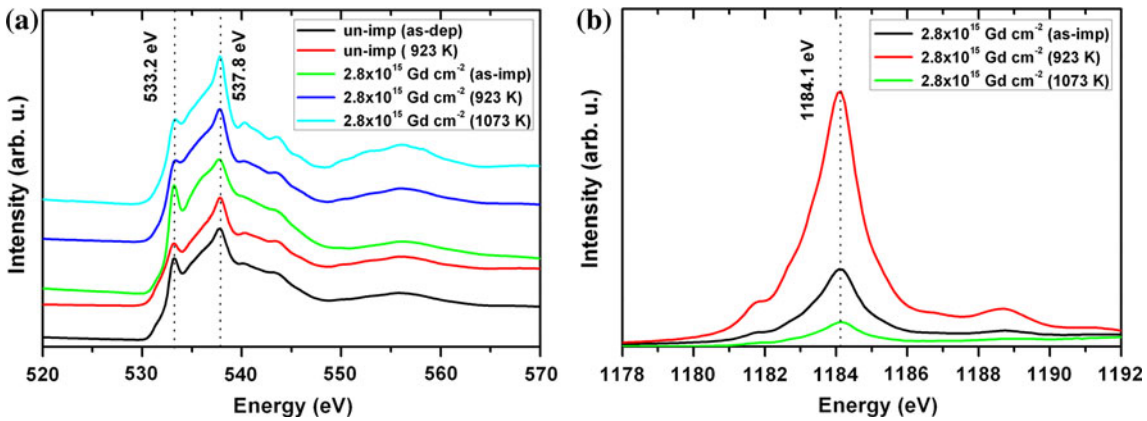

Fig. 7 (Colour online) **a** XANES spectra of O K-edge for un-implanted, 2.8 × 10^{15} Gd cm^{-2} implanted and annealed ZnO films (spectra vertically offset for clarity). **b** XANES spectra of the Gd M_5-edge for 2.8 × 10^{15} Gd cm^{-2} implanted and annealed ZnO films

However, of note is a pre-edge feature at 533.2 eV observed in all of the samples. This peak does not occur in single crystal ZnO, but similar features have been reported in ZnO:Gd [19] and ZnO:Mn [40] and attributed to hybridization between low lying O 2*p* levels and Gd 4*f*/5*d* or Mn 3*d* states. However, the presence of the pre-edge features in our as-deposited and un-implanted 923 K annealed films implies that some other mechanism can be involved. Singh et al. [41] reported that oxygen vacancies can contribute significantly towards the observed pre-edge features. They studied the effect of argon (Ar) implantation into ZnO and annealing in an Ar atmosphere. They observed that the pre-edge features became prominent with increasing Ar concentration, and primarily attributed this to enhanced oxygen vacancies created during implantation and annealing. However, ion implantation is expected to create numerous types of defects, including zinc interstitials, antisite disorder, and in our case Gd atoms bonded to oxygen, and any or all of these could be contributing to the peak at 533.2 eV.

For our samples, the as-implanted ZnO:Gd shows the strongest pre-edge feature implying the highest concentration of the relevant defects, with the peak decreasing considerably upon annealing. As mentioned earlier, mobilisation of oxygen trapped at grain boundaries during annealing can compensate the oxygen vacancies, so the data are consistent with the assumption that the pre-edge feature is at least partially related to oxygen vacancies. Furthermore, as expected annealing helps the films to become more crystalline as seen by sharper peaks around 537.8 eV.

XANES measurements at the Gd $M_{4,5}$ edge can be used to investigate the localised inner 4*f* states. They probe the dipole allowed transitions from the $3d^{10}4f^{7}$ ground state to $3d^{9}4f^{8}$ excited state multiplets. Figure 7b shows the Gd M_5 edge for 2.8×10^{15} Gd cm^{-2} implanted and annealed ZnO films. All of the spectra match with the typical spectrum for Gd^{3+} ions [42]. Similar Gd M_5 edges were observed in Gd doped ZnO films prepared by a pulsed-spray pyrolysis technique [19]. No distinct changes due to annealing were observed in the shape of Gd M_5 edges, but there is a considerably reduced signal in the 1073 K annealed film. We attribute this to migration of Gd ions deeper into the film, so that the near-surface concentration that contributes to the TEY signal is reduced. This is consistent with the RBS results described above.

Conclusions

The structural, electrical and magnetic properties of ZnO:Gd films were investigated at different annealing temperatures. The Gd distribution within the films has been studied by RBS and TEM, which reveal that the Gd distribution is inhomogeneous after annealing, and for the highest annealing temperature the Gd diffuses deeper into the film. Morphological studies by SEM show that the grain sizes increased with increasing annealing temperature from ~10 to ~30 nm. Electrical resistivity and Hall-effect measurements show that annealing increases the film resistivity and decreases the carrier concentration, possibly due to the compensation of oxygen vacancies by de-trapping of oxygen at the grain boundaries. The magnetization data for all annealing temperatures can be interpreted in terms of spatially inhomogeneous magnetic phases that display paramagnetism, superparamagnetism, and ferromagnetism. The paramagnetism is due to isolated Gd moments distributed within the films. The ordered magnetic phase is unclear but it is clearly associated with regions of the films with high Gd concentration. The resultant saturation moment per Gd initially increases and then decreases with increasing annealing temperature. The XANES data have a pre-edge feature at the O K-edge that can be attributed to a range of structural defects in the film rather than to Gd-induced electronic states. The XANES data at the Gd M_5 edge are consistent with Gd valence of 3+.

Acknowledgements We acknowledge funding from the Foundation for Research Science and Technology of New Zealand (C05X0408) and the MacDiarmid Institute. The authors are grateful to the New Zealand synchrotron group and the Soft X-ray Beamline scientist Dr. Bruce Cowie, and other staff at the Australian Synchrotron for their help. The authors acknowledge the assistance provided by Dr. Toby Hopf for SEM, and Dr. Shen Chong and Jibu Stephen for MPMS measurements. J. Leveneur is acknowledged for fruitful discussion of the XANES and MPMS data.

References

1. Wolf SA, Awschalom DD, Buhrman RA, Daughton JM, von Molnar S, Roukes ML, Chtchelkanova AY, Treger DM (2001) Science 294:1488
2. Dietl T, Ohno H, Matsukura F, Cibert J, Ferrand D (2000) Science 287:1019
3. Barzykin V (2005) Phys Rev B 71:155203
4. Jalbout AF, Chen H, Whittenburg SL (2002) Appl Phys Lett 81:2217
5. Coey JMD, Venkatesan M, Fitzgerald CB (2005) Nat Mater 4:173
6. Jungwirth T, Wang KY, Masek J, Edmonds KW, Konig J, Sinova J, Polini M, Goncharuk NA, MacDonald AH, Sawicki M, Rushforth AW, Campion RP, Zhao LX, Foxon CT, Gallagher BL (2005) Phys Rev B 72:165204
7. Ozgur U, Alivov YI, Liu C, Teke A, Reshchikov MA, Dogan S, Avrutin V, Cho SJ, Morkoc H (2005) J Appl Phys 98:041301
8. Sato K, Katayama-Yoshida H (2002) Semicond Sci Technol 17:367
9. Song C, Geng KW, Zeng F, Wang XB, Shen YX, Pan F, Xie YN, Liu T, Zhou HT, Fan Z (2006) Phys Rev B 73:024405
10. Park JH, Kim MG, Jang HM, Ryu S, Kim YM (2004) Appl Phys Lett 84:1338

11. Norton DP, Overberg ME, Pearton SJ, Pruessner K, Budai JD, Boatner LA, Chisholm MF, Lee JS, Khim ZG, Park YD, Wilson RG (2003) Appl Phys Lett 83:5488
12. Bouloudenine M, Viart N, Colis S, Kortus J, Dinia A (2005) Appl Phys Lett 87:052501
13. Golmar F, Villafuerte M, Navarro AM, Torres CER, Barzola-Quiquia J, Esquinazi P, Heluani SP (2010) J Mater Sci 45:6174. doi:10.1007/s10853-010-4710-2
14. de Carvalho HB, de Godoy MPF, Paes RWD, Mir M, de Zevallos AO, Iikawa F, Brasil MJSP, Chitta VA, Ferraz WB, Boselli MA, Sabioni ACS (2010) J Appl Phys 108:033914
15. Khalid M, Ziese M, Setzer A, Esquinazi P, Lorenz M, Hochmuth H, Grundmann M, Spemann D, Butz T, Brauer G, Anwand W, Fischer G, Adeagbo WA, Hergert W, Ernst A (2009) Phys Rev B 80:035331
16. Qi J, Yang Y, Zhang L, Chi J, Gao D, Xue D (2009) Scr Mater 60:289
17. Potzger K, Zhou S, Eichhorn F, Helm M, Skorupa W, Mucklich A, Fassbender J, Herrmannsdorfer T, Bianchi A (2006) J Appl Phys 99:063906
18. Ungureanu M, Schmidt H, von Wenckstern H, Hochmuth H, Lorenz M, Grundmann M, Fecioru-Morariu M, Guntherodt G (2007) Thin Solid Films 515:8761
19. Subramanian M, Thakur P, Tanemura M, Hihara T, Ganesan V, Soga T, Chae KH, Jayavel R, Jimbo T (2010) J Appl Phys 108:053904
20. Shi H, Zhang P, Li SS, Xia JB (2009) J Appl Phys 106:023910
21. Monteiro T, Neves AJ, Carmo MC, Soares MJ, Peres M, Alves E, Rita E, Wahl U (2006) Superlattices Microstruct 39:202
22. Kennedy J, Carder DA, Markwitz A, Reeves RJ (2010) J Appl Phys 107:103518
23. Murmu PP, Kennedy J, Markwitz A, Ruck BJ (2009) AIP Conf Proc 1151:185
24. Kennedy J, Pithie J, Markwitz A (2008) Proc SPIE 6800: 68001P-1
25. Markwitz A, Kennedy J (2009) Int J Nanotech 6:369
26. Biersack JP (1987) Nucl Instrum Methods Phys Res B 27:21
27. Kennedy J, Markwitz A, Trodahl HJ, Ruck BJ, Durbin SM, Gao W (2007) J Electron Mater 36(4):472
28. Doolittle LR (1985) Nucl Instrum Methods Phys Res B 9:334
29. Koskelo O, Räisänen J, Tuomisto F, Eversheimc D, Grasza K, Mycielski A (2010) Thin Solid Films 518:3894
30. Dietl T, Andrearczyk T, Lipińska A, Kiecana M, Tay M, Wu Y (2007) Phys Rev B 76:155312
31. Look DC, Hemsky JW, Sizelove JR (1999) Phys Rev Lett 82:2552
32. Tuomisto F, Saarinen K, Look DC, Farlow GC (2005) Phys Rev B 72:085206
33. Kim YJ, Kim HJ (1999) Mater Lett 41:159
34. Roeland LW, Cock GJ, Muller FA, Moleman AC, McEwen KA, Jordan RG, Jones DW (1975) J Phys F Met Phys 5:L233
35. Reule H, Hirscher M (2000) J Alloys Compd 298:1
36. Wang DH, Huang SL, Han ZD, Su ZH, Wang Y, Du YW (2004) Solid State Commun 131:97
37. Moon RM, Koehler WC (1975) Phys Rev B 11:1609
38. Martinez B, Sandiumenge F, Balcells L, Arbiol J, Sibieude F, Monty C (2005) Phys Rev B 72:165202
39. Preston ARH, Ruck BJ, Piper LFJ, De Masi A, Smith KE, Schleife A, Fuchs F, Bechstedt F, Chai J, Durbin SM (2008) Phys Rev B 78:155114
40. Thakur P, Chae KH, Kim JY, Subramanian M, Jayavel R, Asokan K (2007) Appl Phys Lett 91:162503
41. Singh AP, Kumar R, Thakur P, Brookes NB, Chae KH, Choi WK (2009) J Phys Condens Matter 21:185005
42. Thole BT, van der Laan G, Fuggle JC, Sawatzky GA, Karnatak RC, Esteva JM (1985) Phys Rev B 32:5107